JAAS

Improved Uranium Particle Analysis by SIMS using O3- Primary Ions

SCHOLARONE™
Manuscripts

ARTICLE

Improved Uranium Particle Analysis by SIMS using O_3^- Primary Ions

Evan E. Groopman,*[a] Todd L. Williamson [a] and David S. Simons [b]

We have investigated the use of negative molecular oxygen primary ion beams (i.e., O_2^- and O_3^-) to determine the benefits of using such beams for uranium particle SIMS analyses. Typically, O^- is the most practical negative primary ion species from the conventional duoplasmatron ion source for both age dating and uranium isotopic analysis of particles. Newer RF plasma ion sources make it possible to use O_2^- and O_3^- due to higher brightness and primary ion fluence, and the increased abundance of molecular species in the plasma relative to the duoplasmatron. We have determined that by using an O_3^- beam, the ionization yield can be increased by a factor of approximately two over an O^- beam, up to 4.7%, a substantial improvement that positively impacts measurement precision and detection limits. We also investigated the effect of the molecular oxygen beams on uranium isotope mass fractionation and the Th/U relative sensitivity factor for SIMS analyses in comparison to O^- beams. We found that O_3^- reduced instrumental mass fractionation and matrix/substrate effects relative to the other negative ion beams. Particle measurements using O_3^- were improved compared to conventional O^- beam analyses due to higher yields, smaller corrections, and reduced substrate effects.

Introduction

Particulate nuclear material from environmental samples is routinely analyzed by both bulk and particle mass spectrometry techniques [1-3]. Samples are collected on cotton swipes and then prepared for both microscopic inspection and isotopic analyses typically using thermal ionization mass spectrometry (TIMS) or secondary ion mass spectrometry (SIMS). The distribution of U isotopic compositions from individual microscopic particles can help illustrate information about source material inputs and outputs for an associated set of particles from a specific process. Recently, the National Institute of Standards and Technology (NIST) developed an additional methodology for determining the ages of microscopic U particles by SIMS using the radioactive chronometer pair $^{234}U{:}^{230}Th$, which decays with a half-life of 245,500 ± 600 years[4]. For the analysis of particles that have undergone chemical/material processing, the measured ratio of $^{230}Th/^{234}U$ in a particle will reflect its last purification date. This temporal information complements isotopic analyses for discriminating between past and present material processing by providing an activity timeline.

Uranium isotope and age dating measurements on small and/or young samples require the highest achievable ion yields coupled with low instrument background[4]. Large-geometry (LG)-SIMS instruments have been used to analyze actinides because of their simultaneous high transmission and high mass resolving power (MRP)[4-8]. Electropositive actinides are generally measured with SIMS by sputtering the sample with a reactive primary ion beam, usually O^-, O_2^+, or O_2^-. These primary species are produced in the conventional duoplasmatron and newer radio-frequency (RF) ion sources. The achievable ion current of O_2^+ is higher than O^-, but the impact energy at the sample surface and resulting secondary ion yields are higher using O^- and O_2^-. Experiments with other polyatomic and reactive primary ion species (e.g., F^-, $NO_2^\pm$, $N_2O_2^-$, CFO^-, CF_3^-) produced in the duoplasmatron have shown increased secondary ion yields relative to both O^- and O_2^+ [9-11]. The useful yield is defined as the number of ions detected relative to the number of atoms removed from the sample. A high useful yield requires both high transmission through the mass spectrometer and efficient conversion of sputtered atoms into measurable ion channels, such as U^+. Low ionization and/or production of unwanted secondary signals, such as UO_2^+, can reduce the overall useful yield. In SIMS, the ionization rates of elements are impacted by the local sample surface chemistry, which includes the relative abundances of other constituents and the implanted primary ions. These are broadly referred to as "matrix effects". Instantaneous ion yields are a product of these matrix effects, and are also affected by the primary beam current, sputter rate, and sample crystallography. The sputtering process is highly linear, so the integrated counts under low and high primary beam currents are generally equivalent, bounded by the effects of the local chemical environment and the signal-to-noise ratio. Therefore, the useful yield of an element is highly sample and/or substrate dependent. To measure precise inter-element abundances, the relative sensitivity factor (RSF), or relative ionization rate, of those elements must be measured in a relevant standard.

A positively biased sample is required to analyze electropositive elements and their most abundant sputtered ions, such as U^+. This

a. Materials Measurement Science Division, National Institute of Standards and Technology, Gaithersburg, MD, 20899, USA
b. MELE Associates, Inc., Rockville, MD, 20850, USA
*evan.groopman@nist.gov
ORCID: 0000-0002-7842-3295, 0000-0001-8001-7790, 0000-0001-5719-836X

sample voltage affects the impact energy of primary ions, their penetration depth, and their secondary ion yield. For example, an O^- primary beam accelerated to -13 kV will impact the +10 kV biased sample with 23 keV of energy. A comparable O_2^+ beam accelerated to +15 kV will only impact a +8 kV biased sample with 7 keV of energy.

The Hyperion-II RF plasma ion source (Oregon Physics, LLC, Beaverton, OR, USA) has several well-known advantages relative to the duoplasmatron, most notably: 3-10× beam brightness (ion density) and current, and lower energy dispersion [12, 13]. In addition, the RF source produces a larger fraction of negative molecular primary ion species, such as O_2^- and O_3^-. Typically, a magnetic sector (primary beam mass filter, PBMF) or Wien filter on the primary ion column is used to select the primary species impacting the sample. On the LG-SIMS located at NIST, the duoplasmatron produced approximately 85% O^-, 14% O_2^-, and <0.5% O_3^- using a pure O_2 feed gas, whereas the RF source produced roughly 67% O^-, 20% O_2^-, and 13% O_3^-. In practice, therefore, a maximum focused and collimated primary ion current of 200 nA O^- from the duoplasmatron corresponds to only 35 nA O_2^- and 1 nA O_3^-. Using a semi-magnetic anode on the duoplasmatron can increase the extractable O_2^- current [14], but it does not improve O_3^- production in the plasma. Under Köhler illumination conditions [15], these beams are defocused to provide a uniform illumination of the sample, collimated by the final primary beam aperture (e.g., 200 μm in size), so the maximum effective primary ion current at the sample can be 5-10× less than when critically focused. The relatively low Köhler primary ion currents of O_2^- and O_3^- from the duoplasmatron do not typically enable age dating measurements. In contrast, the RF ion source has produced focused beams of at least 1000 nA O^-, 300 nA O_2^-, and 200 nA O_3^- at the sample on the NIST SIMS, or defocused Köhler beams on the order of 200 nA O^-, 60 nA O_2^-, and 35 nA O_3^- into a 50 μm spot. The ion currents of all these species are of a useful magnitude for age dating and isotopic measurements.

Köhler illumination is often used for (non-imaging) analyses of well-separated particles because it provides a uniform current density across the sample over an area much larger than the particle itself. Some of the benefits of this method include: 1) a large analysis area whereby redeposited sputtered neutral atoms have an additional chance to be ionized, improving the total yield; 2) reduced need for pixel-by-pixel deadtime corrections because the count rate is averaged across the analysis area. In SIMS, typically >95% of the sputtered atoms are neutrals that are redeposited on the substrate surface, so any additional chance to ionize them can increase the measurement efficiency. The drawbacks of this method are that it lacks particle-scale spatial information and cannot easily distinguish and exclude signals from nearby particles. Under Köhler illumination (or a comparably large raster of a focused ion beam), most of the sputtered material is the substrate, not the particle of interest. For example, the areal fraction of a 2 μm particle under a 50 μm Köhler beam is only 0.16%, and a 1 μm particle only 0.04%. Therefore, the chemical interactions of the primary beam with the substrate material and the redeposited sputtered neutrals mixed into the substrate can lead to matrix effects, which impact secondary ion yields. The size of the Köhler spot (or rastered Gaussian beam) can also affect the cumulative useful yield based upon the extent of redeposited material around the particle. A small beam size will

result in a lower useful yield. For the work in this paper, a Köhler spot size of 50 μm was used for all measurements.

Experimental

For this work, a CAMECA IMS-1270E7 (upgraded to IMS-1280 equivalence) LG-SIMS (CAMECA Instruments, Inc., Fitchburg, WI, USA) equipped with a Hyperion-II RF plasma ion source was used [13].

Secondary Ion Yields using O^-, O_2^-, O_3^-

Two monodisperse U particle samples were used to calculate the ionization efficiency of U under Köhler bombardment and to investigate substrate dependence: IRMM 2329P (3.58 pg ± 0.67 pg (2σ), 1.3 μm diameter [16, 17]) on vitreous carbon (from Ted Pella, Inc., Redding, CA, USA; density = 1.42 $g \cdot cm^{-3}$) and inkjet-printed U deposits developed at NIST (3 μm diameter) on ultrapure Si (<100> orientation, 2.33 $g \cdot cm^{-3}$). IRMM 2329P particles were produced by vibrating orifice aerosol generation (VOAG). Inkjet printed samples were deposited as uranyl nitrate droplets and calcined to U_xO_y. The IRMM 2329P U mass corresponds to (9.06 ± 1.7) ×10⁹ U atoms per particle (2σ). The mass of the inkjet deposits is not certified, so we did not directly calculate useful yields, but we did compare the relative efficiencies of the three primary species. The reproducibility of the number of U atoms in the inkjet deposits was ≈3% (1σ) when measured by SIMS, but the absolute mass is not well known at this time. Particles were completely consumed while monitoring only the $^{238}U^+$ signal on the monocollector electron multiplier (EM) in cycles of 2 s. No wait times were used between cycles because peak jumping was not required; however, additional delays between cycles were reported in the data time stamps. These were typically between 80 ms and 200 ms per cycle. During these times, the instrument software kept the primary beam on, sputtering the sample. The duty cycles of the full measurements were 94.6%, which were used to compute the useful yields from each particle's integrated counts.

The LG-SIMS was tuned to a mass resolving power (MRP, M/ΔM at 10% peak height) of 2000 for high transmission in "XY" mode (Table 1). The entrance slit was 250 μm, field aperture (FA) 8000 μm, energy slit 50 eV (5117 μm), and exit slit 500 μm. All measurements used a 400 μm contrast aperture. The 50 μm × 50 μm field-of-view (FOV) set by the ion transfer optics was entirely visible through the FA. The primary ion currents at the sample were 12 nA O^-, 7 nA O_2^-, and 4 nA O_3^- through the 200 μm L4 primary beam aperture (50 μm illumination area), which resulted in comparable sputter rates for each probe species.

Comparison of O^-, O_2^-, and O_3^- for U-Th Age Dating and U Isotopic Analyses

Particles of NIST/NBL Certified Reference Material (CRM) U900 on graphite (Ted Pella, Inc., (1.58-1.63) $g \cdot cm^{-3}$) and Si substrates were used to compare the performance of each primary species with respect to $^{230}Th/^{234}U$ radiochronometry and U isotopic analyses. The relative sensitivity factor (RSF) of Th^+/U^+ was measured, in addition to the U isotope instrumental

ARTICLE

Table 1: Measurement Conditions

Parameter	Monocollection (M/ΔM = 2000)	Monocollection (M/ΔM = 3500)	Multicollection (M/ΔM = 2000)
Köhler Spot Size (µm)	50		
Primary L4 Aperture (µm)	200		
Accelerating Voltage (kV)	-13		
Sample Voltage (kV)	+10		
Impact Energy (keV)	23		
Field of View	50 µm × 50 µm		
Entrance Slit (µm)	250	175	200
Field Aperture (µm)	8000	6000	
Contrast Aperture (µm)	400		
Energy Slit (eV)	50	50 (energy scans: 10, 25)	
Exit Slit (µm)	500	250	500
Tuning Mode	XY	XY	CIRC
Detector(s)	EM	EM	L1/C/H1
Detector Dead Time (ns)	27.5	27.5	70/71.7/71.4
Discriminator Threshold (mV)	75	75	75/75/75
Application	*U^+ yield*	*Chronometry ($^{230}Th/^{234}U$), U isotopes*	*$U^+/UO^+/UO_2^+$ yield*
Samples	*IRMM 2329P, inkjet printed U deposits*	*CRM U900, uraninite ore*	*CRM U900, IRMM 2329P, inkjet printed U*

mass fractionation. Szakal et al. (2019) [4] describe these measurement methods in detail, so we only briefly recount them here. The LG-SIMS was tuned with a MRP ≈3500 in "XY" mode on the monocollector EM (Table 1). The FA was 6000 µm, which optically gated the maximum 50 µm × 50 µm FOV to 37.5 µm × 37.5 µm. Therefore, secondary ions from the edges of the 50 µm Köhler spots were rejected from the mass spectrometer. The entrance slit was 175 µm, energy slit 50 eV, and exit slit 250 µm. Primary ion currents between 4 and 20 nA were used for each beam species, with most approximately 10 nA.

For Th/U RSF analyses, we measured $^{207}Pb^{23}Na^+$, $^{230}Th^+$, and $^{234}U^+$ serially by peak hopping the magnetic sector, counting for 2.00 s, 20.00 s, and 2.00 s, respectively. Count times were preceded by respective waiting times of 2.00 s, 0.96 s, and 0.96 s, to allow the magnetic field to settle. Each measurement lasted 20 cycles, in line with previous work [4]. Prior to each measurement, we cycled the magnetic field 10 times to establish a hysteresis loop and then centered all three masses by scanning the $^{234}U^+$ peak and applying a uniform offset to the preset field locations.

The best known purification date for CRM U900 was January 24, 1958 [18, 19], making it approximately $t ≈ 65.25$ years old as of these analyses. With λ_{234} = 2.823×10⁻⁶ decays/year, the approximate $^{230}Th/^{234}U$ ratio during these measurements was $\lambda_{234} \cdot t ≈ 1.842×10^{-4}$. The Th/U RSF was calculated as

$$\mathrm{RSF_{Th/U}} = \frac{N_{230}^+/N_{234}^+}{\lambda_{234} \cdot t} \quad \#(1)$$

where N_i^+ denotes the integrated counts for isotope i, and t reflects the analysis date for each sample.

Following Th/U RSF analysis of each particle, uranium isotopes and $^{232}Th^+$ were measured serially as $^{232}Th^+$, $^{234}U^+$, $^{235}U^+$, $^{235}U^1H^+ + ^{236}U^+$, $^{238}U^+$, $^{238}U^1H^+$ for 2.00 s, 4.96 s, 1.04 s, 4.00

s, 3.04 s, and 4.00 s, respectively. The hydride interference on $^{236}U^+$ was corrected by using the $^{238}U^1H^+/^{238}U^+$ ratio[20]. Wait times of 0.96 s were used to switch between masses, except before ^{232}Th, which had a wait time of 2.00 s. Before each measurement, 10 magnet cycles were used to establish a hysteresis loop, after which $^{235}U^+$ was used as a centering reference for all isotopes. Beam currents between 300 pA and 2 nA were used, depending on the primary ion species and particle size. In all cases the count rate of the most abundant isotope, $^{235}U^+$, was targeted to be at or slightly below $2×10^5$ counts·s⁻¹.

Particles of uraninite ore from Topsham, Maine, were deposited on a graphite substrate to investigate the effects of primary ion species on the energy distributions of $^{238}U^+$ and $^{232}Th^+$. The ^{230}Th abundance in CRM U900 was not high enough to produce a sufficiently intense energy scan signal. The absolute abundances of U and Th were not known in the uraninite *a priori*, however primary ion currents were chosen to yield approximately $1×10^5$ counts·s⁻¹ at their maxima. The nominal sample voltage was +10 kV. Energy scans were performed by applying offsets to the nominal sample voltage between -100 V and +50 V with the energy slit fixed at widths of 10 eV, 25 eV, and 50 eV. Ions ejected from the sample surface with low energy were accelerated by the 10 kV electric field between the positively biased sample and the grounded extraction plate, resulting in approximately 10 keV of kinetic energy. Ions ejected with higher energy from the sample had comparably higher kinetic energies entering the mass spectrometer. By applying a negative offset to the sample voltage, the acceleration was reduced, so higher-energy ions entered the mass spectrometer with the nominal sample voltage. Under high-vacuum conditions, there was essentially no low-energy side to the energy distribution (ions cannot be ejected with negative kinetic energy). However, scattering of
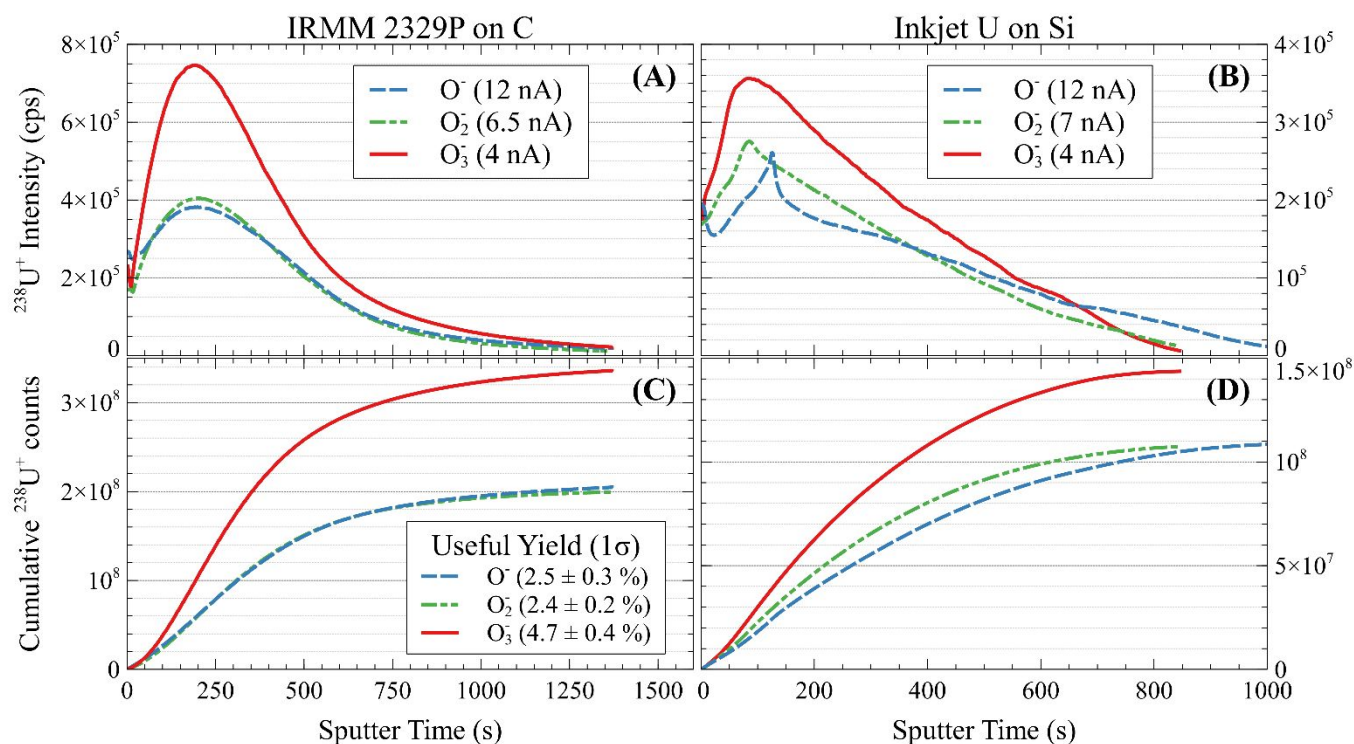
Figure 1: Characteristic sputter profiles of IRMM 2329P particles on vitreous carbon and inkjet-printed deposits on Si (M/ΔM = 2000). (A) Sputter profiles of IRMM 2329P particles under O^- (12 nA, blue dashed), O_2^- (6.5 nA, green dot-dashed), and O_3^- (4 nA, red solid) bombardment. Beam currents were chosen to produce similar sputter rates. (B) Sputter profiles of inkjet deposits under similar conditions. The sharp peaks in the O^- and O_2^- profiles were due to the transformation of the Si substrate to SiO_x ($x < 2$). O_3^- bombardment avoided this behavior due to a shallower implantation depth. (C) Cumulative count profiles for IRMM 2329P, equivalent to useful yields of 2.5 ± 0.3 %, 2.4 ± 0.2 %, and 4.7 ± 0.4 % for O^-, O_2^-, and O_3^-, respectively. (D) Cumulative profiles for inkjet deposits. The standard deviation of the integrated profiles were ≈9% for IRMM 2329P (the certified mass uncertainty) and ≈3% for the inkjet deposits.

Table 2: Absolute and relative useful yields of U^+ from IRMM 2329P on carbon and inkjet-printed deposits on Si. The inkjet mass was not certified, so absolute yields were not calculated. Uncertainties are 1σ. The uncertainty on the certified mass of IRMM 2329P (≈9%) was the primary component of the useful yield uncertainty.

Sample	O^- (%)	O_2^- (%)	O_3^- (%)	O_2^-/O^-	O_3^-/O^-
IRMM 2329P on C	2.5 ± 0.3	2.4 ± 0.2	4.7 ± 0.4	1.0 ± 0.1	1.9 ± 0.3
Inkjet on Si	--	--	--	1.1 ± 0.1	1.5 ± 0.2

ejected ions with gas phase atoms or molecules in the sample chamber can result in energy loss, such as when using oxygen flooding or under poor vacuum conditions. For these measurements, oxygen flooding was not used, and the typical vacuum pressure in the sample chamber was approximately 1.3×10^{-8} Pa (1×10^{-10} torr, 1.3×10^{-10} mbar).

Comparison of U^+, UO^+, and UO_2^+ yields using O^-, O_2^-, and O_3^-

The multicollector on the LG-SIMS was used to simultaneously measure $^{238}U^+$, $^{238}U^{16}O^+$, and $^{238}U^{16}O_2^+$ from CRM U900 on graphite and Si, IRMM 2329P on vitreous carbon, and the inkjet particles on Si. Prior experience has shown that O^- and O_2^- bombardment on Si caused a sudden change in the secondary ion intensities as the matrix oxidized to SiO_x ($x < 2$) [6, 21, 22]. This transition occurred rapidly, with the U^+ signal dropping by 25% over the course of ≈20 s with a 12 nA O^- beam. At the same time, the matrix transition caused the yields of UO^+ and UO_2^+ to increase. Using multicollection obviated the need for time interpolation of the cycles, which can be challenging to perform well for rapidly changing signals, and it improved the

precision of molecular useful yield measurements. Peak jumping +16 m/z and -32 m/z would have required waiting and cycle times that would have reduced the resolution of this transition and resulted in low duty cycles. Cycles of 2 s were used, as before.

Three detector trolleys (L1: $^{238}U^+$, C: $^{238}U^{16}O^+$, H1: $^{238}U^{16}O_2^+$) were used for these measurements, with the axial mass of the magnetic sector tuned to $^{238}U^{16}O^+$. The trolley positions were 27320 µm, 205310 µm, and 50480 µm, respectively. UO^+ was used to calculate the yield balance factors for each detector. Dead times for the detectors were set at 70 ns, 71.7 ns, and 71.4 ns.

Statistical Analyses

When reporting the weighted mean (WM) of a dataset in this paper, we used the *unbiased* standard error of the weighted mean (SE_{WM}), as described by Kirchner [23] and Meier [24]. This provided an expanded uncertainty about the WM when the individual data weights (inverse variances) were not equal and therefore the effective degrees of freedom, n_{eff}, were fewer
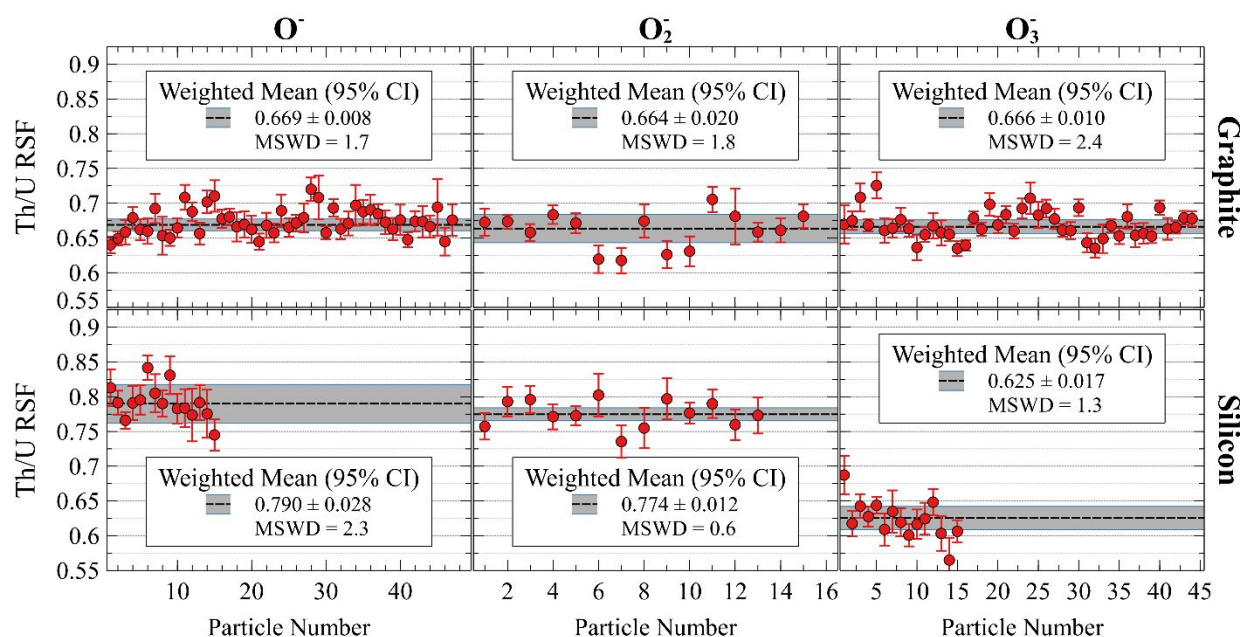
Figure 2: Th/U RSF measured on CRM U900 using O⁻, O₂⁻, and O₃⁻ on graphite and Si. As with the depth profiles, O₃⁻ reduces matrix effects, yielding an RSF that is more similar between graphite and Si than the other beams.

Table 3: Weighted mean Th/U RSF values for measurements of CRM U900 particles on graphite and silicon using O⁻, O₂⁻, O₃⁻. For each substrate, the first row shows the weighted mean, standard error of the weighted mean (SE_{WM}), 95% confidence intervals (CIs) equivalent to the SE_{WM} × t-factor × √(MSWD), and (≈2×) unbiased weighted standard deviation (SD_W). The second row shows the bias-corrected and accelerated weighted bootstrap resampling of the weighted mean with 95% CIs. The bootstrap resampling showed good agreement with the analytical values, though the 95% CIs were usually slightly smaller. "--" indicates no value given.

Substrate	O⁻	SE_{WM}	95% CI	2 SD_W	O₂⁻	SE_{WM}	95% CI	2 SD_W	O₃⁻	SE_{WM}	95% CI	2 SD_W
Graphite	0.669	0.003	0.008	0.037	0.664	0.007	0.020	0.046	0.666	0.003	0.010	0.036
bootstrap	0.669	0.003	0.007	--	0.664	0.008	0.015	--	0.666	0.003	0.006	--
Silicon	0.790	0.008	0.028	0.053	0.774	0.005	0.012	0.035	0.625	0.007	0.017	0.044
bootstrap	0.790	0.008	0.018	--	0.774	0.005	0.011	--	0.625	0.006	0.013	--

than the number of data points, n. A description and multiple examples are provided in the Supplemental Information. Confidence intervals (95%) around the WM were constructed by multiplying the SE_{WM} by the Student's t-factor, $t_{\alpha/2,n_{eff}-1}$, and by the square root of the mean squared weighted deviation (MSWD, also known as the reduced chi-square statistic) [25]. These expansions of the error about the WM account for the additional uncertainty of estimating the population variance from a finite number of points, and for the real scatter in the data. When MSWD < 1, √MSWD was omitted to provide conservative CI estimates. For example, $t_{\alpha/2,n-1}$ = 2.26 when n = 10 and α = 0.05, i.e., the 97.5th percentile of the Student's t-distribution with 9 degrees of freedom. As $n \to \infty$, $t \to 1.96$ for α = 0.05. For the weighted MSWD and Student's t-value, n_{eff} -1 was used as the degrees of freedom. The results for the weighted means were verified using the bias-corrected and accelerated bootstrap resampling algorithm [26] with weighted resampling. Weights for the resampling were taken to be the normalized inverse square uncertainties on the data. The probability of drawing a data point during resampling with replacement was equivalent to its weight. Therefore, for data sets with unequal uncertainties, the effective degrees of freedom were reduced, as in the unbiased weighted mean.

Linear regressions were performed using the York method with correlated uncertainties on both axes, where applicable [27, 28]. Python code to perform the fits was adapted from [29]. Ion yield uncertainties were calculated as the standard error of the mean of several measurements, and, where applicable, were summed in quadrature with the certified mass uncertainty of IRMM 2329P particles.

Results

Comparison of Secondary Ion Yields using O⁻, O₂⁻, and O₃⁻

Figure 1A shows characteristic sputter profiles of IRMM 2329P particles on a vitreous carbon planchet with MRP = 2000. Panel C shows the cumulative ²³⁸U⁺ counts from each profile, with total U ion yields of 2.5 ± 0.3 % for O⁻ (blue dashed), 2.4 ± 0.2 % for O₂⁻ (green dot-dashed), and 4.7 ± 0.4 % for O₃⁻ (red solid). O₃⁻ produced nearly 90% more ions than O⁻ for U particles on graphite. The certified mass uncertainty on the IRMM 2329P particles was 9.4% (1σ) [16]; this was the largest component of the useful yield uncertainties. The standard deviation of our measurements in nearly every case was smaller than 9.4%. All profiles varied smoothly during sputtering. Primary currents of
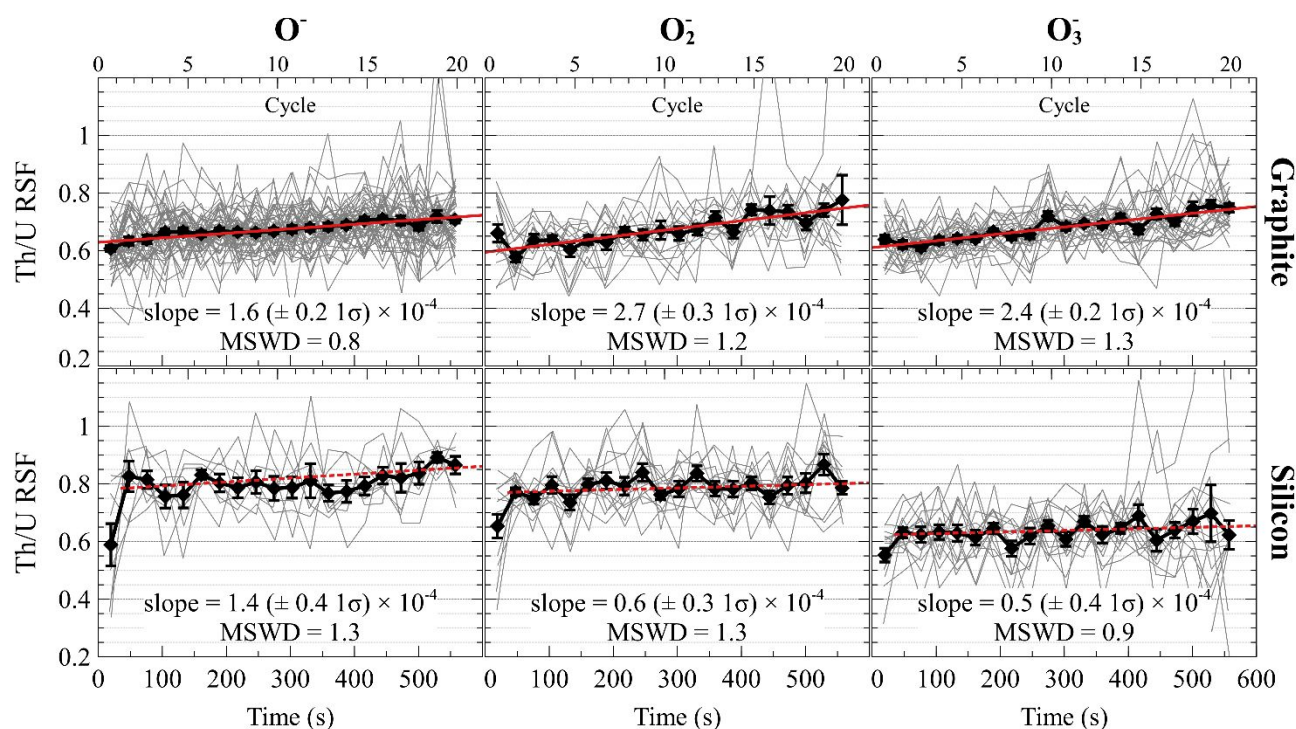
O^- O_2^- O_3^-

Figure 3: Th/U RSF profiles in CRM U900 particles on graphite and Si.

12 nA, 6.5 nA, and 4 nA resulted in similar sputter rates, illustrating the ≈3× sputter rate of O_3^- relative to O^- at the same nominal ion current. Under higher mass resolving power (MRP = 3500) conditions used for U/Th age dating, the U^+ ion yields were 2.1 ± 0.2 % for O^-, 2.1 ± 0.2 % for O_2^-, and 3.9 ± 0.4 % for O_3^- (profiles not shown). Remarkably, the yield from O_3^- under higher MRP (3500) was 60% larger than that from O^- and O_2^- under lower MRP (2000) conditions, where instrument transmission was approximately 30% higher.

Figure 1B,D shows characteristic sputter profiles of the inkjet-printed U deposits. O_3^- produced the highest ion yield of U, approximately 50% more than O_2^- and O^- (Table 2). O_3^- produced the most smoothly varying profiles, which were not sharply peaked. Here and previously, O^- resulted in a depth profile with rapid changes in ion intensity, likely due to crystallographic transitions in the Si due to O implantation [6]. These phase transitions can be problematic for any monocollector measurement of several isotopes where time interpolation would be required. These contrast the depth profiles on C substrates, which all evolved smoothly. O_2^- resulted in a less abrupt profile change than O^- on Si, but was less ideal than O_3^-.

The comparative behavior of the three beams was likely due to the difference in implantation depth. Polyatomic species deposit their energy closer to the surface, whereas monoatomic species cause collision cascades and amorphization deeper into the sample. The implantation depth scales with the projectile energy and inversely with the mass. For polyatomic projectiles, the energy would be partitioned equally between its constituent atoms on impact, so a 23 keV O_3^- ion effectively becomes three 7.66 keV O atoms bombarding the sample.

However, the energy density per impact would be much higher than a conventional beam of O^- ions with 7.66 keV since the three constituent atoms arrive simultaneously at the same location. This is the same principle behind large cluster ion sources on time-of-flight (ToF) SIMS instruments, where monolayer depth resolution is highly desirable.

Comparison of O^-, O_2^-, and O_3^- for Age Dating Analyses

Figure 2 shows the Th/U relative sensitivity factor (RSF) measured on CRM U900 with the three primary beam species. Table 3 shows the weighted mean values for each permutation, the 95% confidence interval about the mean, and 2× the unbiased weighted standard deviation of each sample set. The RSFs on graphite were identical between O^-, O_2^-, and O_3^-, within uncertainties. For O^- 47 particles were measured, which yielded an RSF of 0.669 ± 0.008 (95% CI), with n_{eff} = 35.5 and MSWD = 1.7. For O_2^- 15 particles were measured, which yielded an RSF of 0.664 ± 0.020 (95% CI), with n_{eff} = 11.1 and MSWD = 1.8. For O_3^- 44 particles were measured, which yielded an RSF of 0.666 ± 0.010 (95% CI), with n_{eff} = 33.8 and MSWD = 2.4. The MSWD for O_3^- was larger than for O^- and O_2^- in part because of the smaller analytical uncertainties associated with each analysis. The unbiased weighted standard deviations were similar between the three beams.

The Th/U RSF on Si varied considerably with primary beam species relative to graphite. The RSFs under O^- and O_2^- bombardment were equivalent within uncertainties, with weighted average values of 0.790 ± 0.028 (95% CI, n=15, n_{eff} = 10.4, MSWD = 2.3) and 0.774 ± 0.012 (95% CI, n=13, n_{eff} = 10.4, MSWD = 0.6), respectively. These were approximately 16–18% higher than on graphite. In contrast, the RSF under O_3^- bombardment was 6-7% lower than on graphite, with a mean
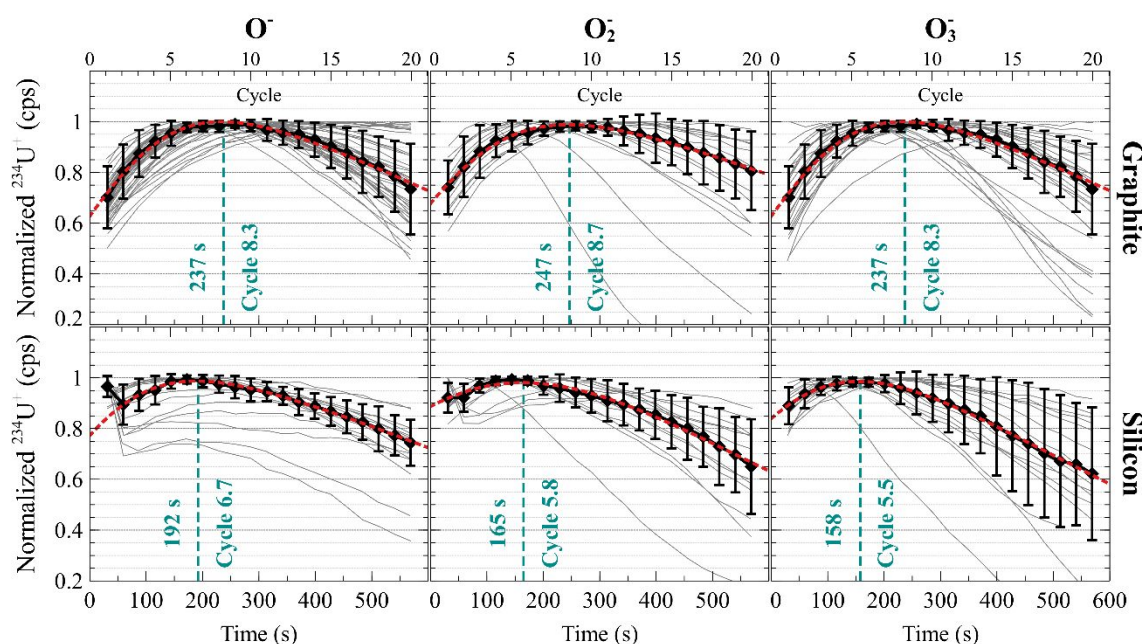
ARTICLE

Figure 4: Normalized $^{234}U^+$ profiles from U900. Differences in particle size are mostly responsible for the varying sputter profiles (gray). The black curve (diamonds) shows the biweight location (robust center) of the distribution of profiles with uncertainties corresponding to the median absolute deviation at each cycle. A skew-normal curve (red dashed line) was fit to the profiles to facilitate a qualitative comparison of the profile shapes.

value of 0.625 ± 0.017 (95% CI, n=15, n_{eff} = 11.5, MSWD = 1.3). The difference in these values may be attributable in part to the conversion of Si to SiO_x under O^- and O_2^- bombardment, as described above. The shallower implantation of O_3^- may result in an RSF more indicative of Si than SiO_x.

Figure 3 shows the evolution of the Th/U RSF over the 20 cycle-long measurements (≈600 s). The trend for each measurement is shown in grey, and the cycle-by-cycle averages are shown in black with error bars corresponding to the unweighted standard error of the mean. Since there were slight timing differences in the measurements due to computer computation time, the SD of the times at each cycle was taken for the uncertainty in x. The results from linear regressions are shown in red. For the Si trends, the first cycle was omitted from the regressions, as they tended to be lower than the other cycles. Overall, the rate of Th/U RSF change was higher on graphite than on Si. On graphite, the Th/U RSF tended to monotonically increase over the course of the measurement. On Si there was a rapid change during the first two cycles followed by a plateauing of the trend. This rapid initial change on Si appears to become less significant as the primary ion mass increases, potentially indicating a minimization of the matrix-induced effects of Si. Interestingly, the RSF from the first cycle of O^- and O_2^- is similar to the average value for O_3^- and the first cycle on graphite. This may be more indicative of the RSF on Si prior to oxidation to SiO_x. For each substrate the trends for O_2^- and O_3^- had similar slopes. On graphite, O^- exhibited a lesser rate of change than the other beams; this was reversed on Si. The impact of the varying Th/U RSF on the mean value naturally depended on the total counts in each cycle.

Figure 4 shows the $^{234}U^+$ count rate profiles for each measured particle normalized to its maximum (gray lines). Variations in the profile shapes were primarily due to particle size (or sampling multiple particles). The cycle-by-cycle biweight

location of the profiles is shown in black, with error bars corresponding to the robust standard deviation, equivalent to approximately 1.4826 times the median absolute deviation [30]. These provide robust estimators of the central profile within the distribution and its variance with respect to time. For a qualitative comparison between the profiles, a skew-normal distribution was fit to the unweighted central profiles (red dashed curve) and the maximum was numerically calculated [31]. The maxima are indicated by dark cyan vertical dashed lines. Note, the skew-normal fit to the Si O^- data omitted the first cycle, which was an outlier, as in Figure 3. On graphite, the maxima were temporally similar, occurring during cycle 8 (≈240 s), on average. On Si, the maxima tended to occur 2-3 cycles earlier (≈50 − 80 s). These profile patterns implicitly affect the weighting applied to the Th/U RSF trends shown in Figure 3 when the RSF is calculated. For O^- and O_2^- on Si, many of the profiles begin with high $^{234}U^+$ count rates, which drop by 10 − 30% after a couple of cycles. This behavior was not apparent on graphite or with O_3^-. Differences in the sputter rates of graphite and Si substrates were not explored here and may have some impact on these profile shapes.

Comparison of O^-, O_2^-, and O_3^- for U Isotopic Analyses

Figure 5 shows three-isotope plots of uncorrected $^{235}U/^{238}U$ vs. $^{234}U/^{238}U$ deviations from the CRM U900 certificate values for each of the primary beams and substrates. These uncorrected data illustrate the instrumental mass fractionation for each combination. Red error ellipses show 1σ uncertainties on the individual measurements; the filled, solid black and dashed black ellipses shows the 1σ standard error and 95% confidence interval about the WM, respectively. Table 4 shows the mass fractionation calculated from the $^{234}U/^{238}U$ and $^{235}U/^{238}U$ ratios in ‰/amu. At the 95% confidence level there was a distinct difference between the two substrates, with
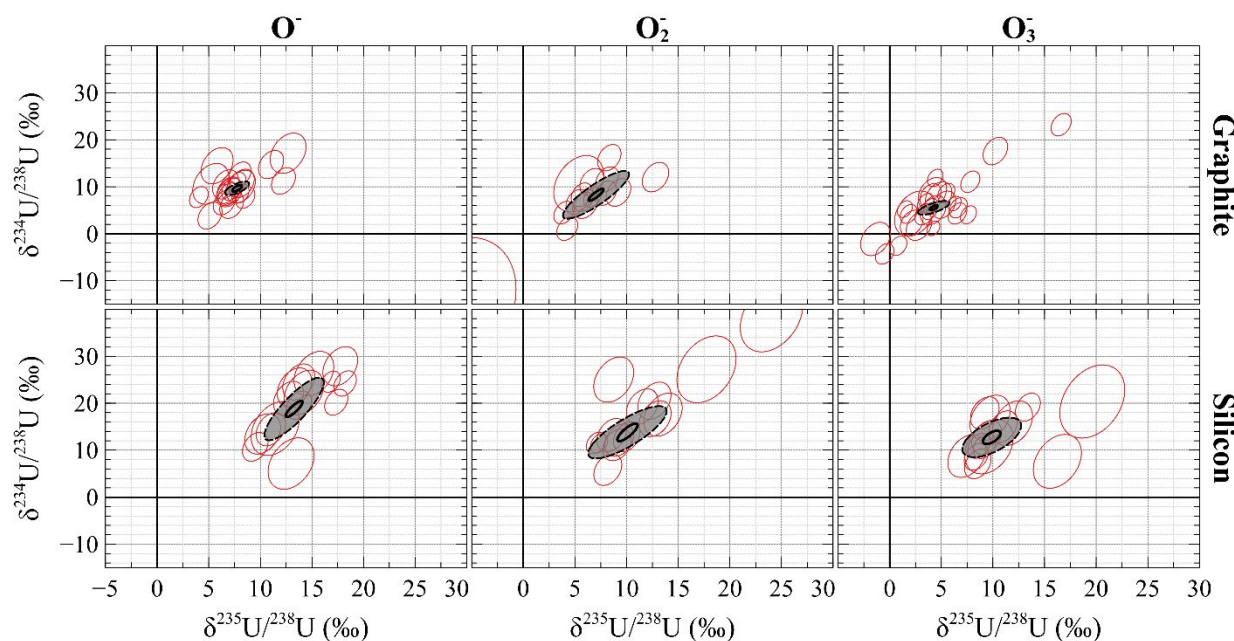
Figure 5: Three-isotopes plots of $^{235}U/^{238}U$ vs. $^{234}U/^{238}U$ isotopic mass fractionation (bias) of CRM U900 particles on graphite and Si under O⁻, O₂⁻, and O₃⁻ bombardment. Red error ellipses show 1σ uncertainties on individual measurements; the filled, solid black and dashed black ellipses shows the 1σ standard error and 95% confidence interval about the WM, respectively. On both substrates O⁻ and O₂⁻ result in larger fractionation relative to O₃⁻. In general, the mass fractionation on Si is ≈2× larger than on graphite.

Table 4: Mass fractionation calculated from the $^{234}U/^{238}U$ and $^{235}U/^{238}U$ ratios (‰/amu). See Figure 5.

Substrate	O⁻	1σ	95% CI	O₂⁻	1σ	95% CI	O₃⁻	1σ	95% CI
Graphite	2.6	0.1	0.2	2.3	0.2	0.6	1.5	0.1	0.3
Silicon	4.6	0.2	0.7	3.5	0.3	0.8	3.4	0.2	0.5

fractionation being ≈2× higher on Si than on graphite. Generally, O₃⁻ resulted in the lowest mass bias and O⁻ the largest. On graphite, the mass fractionations for O⁻, O₂⁻, and O₃⁻ were 2.6 ± 0.1 ‰/amu (1σ), 2.3 ± 0.2 ‰/amu, and 1.5 ± 0.1 ‰/amu, respectively. On Si these were 4.6 ± 0.2 ‰/amu (1σ), 3.5 ± 0.3 ‰/amu, and 3.4 ± 0.2 ‰/amu. The $^{236}U/^{238}U$ ratios were not used to calculate the mass bias because of their lower statistical precision and that they were inferred using a hydride correction from measurements of $^{238}U^1H^+/^{238}U^+$ [20]. The inferred $^{236}U/^{238}U$ ratios retain too much variance for an accurate mass bias calculation at the permil-per-amu level.

Figure 6 shows the energy spectra of $^{238}U^+$ and $^{232}Th^+$ in uraninite with energy slit widths of 10 eV (top) and 25 eV (bottom). For visual comparison, the profiles were normalized to a maximum count rate of 2×10⁵ counts·s⁻¹. The right column shows the ratio of the normalized Th/U signals. For both U and Th, there was a reduction in the high-energy tail with increasing projectile mass, trending from O⁻ to O₃⁻, however this reduction was more significant for U than for Th. As the ion energy increased, the Th/U ratio was greater than 1 for all primary beam species until approximately 30 eV, after which the Th/U ratio for O⁻ dropped below 1. Beyond this point the Th/U ratio tended to increase or plateau for the other beams.

The narrower energy distributions for O₃⁻ and O₂⁻ may impact the observed U isotope mass fractionation. Within the 50 eV energy window used for isotope ratio and age dating measurements, the average ion energies would be slightly different between the three primary species. For example, the relative fraction of low-energy U⁺ ions (-5 eV to +15 eV) with respect to the area under the distributions within the energy slit window (-5 eV to +45 eV) was 73% for O⁻, 78% for O₂⁻, and 82% for O₃⁻. This contrasts the expected behavior using an inverse-velocity-dependent mass fractionation model where heavier isotopes are more depleted in the secondary signal due to their lower velocities [32]. In these previous findings, the mass fractionation was reduced for the higher-energy component of the secondary distribution. Here the heavy isotope depletion was lower for O₃⁻ than for the other primary beams, despite having a narrower and lower average energy distribution. All

three beams impacted the sample at the same angle. O_3^- has an intrinsically higher sputter rate than O^- per nA of primary current. Due to particle size differences, we used a range of primary currents to measure the U isotope compositions, from an average primary current of ≈450 pA for O_3^- to 2.3 nA for O^-. However, we found no correlation between the sputter rate and fractionation as has been found in oxygen isotopes from bulk glasses [33]. These findings warrant further investigation into the behavior of secondary ion formation under bombardment from molecular ion beams. Specifically, mass fractionation measurements at different sample voltage offsets with a narrow energy slit (e.g., 2 eV), and for several elements, may illuminate the behavior.

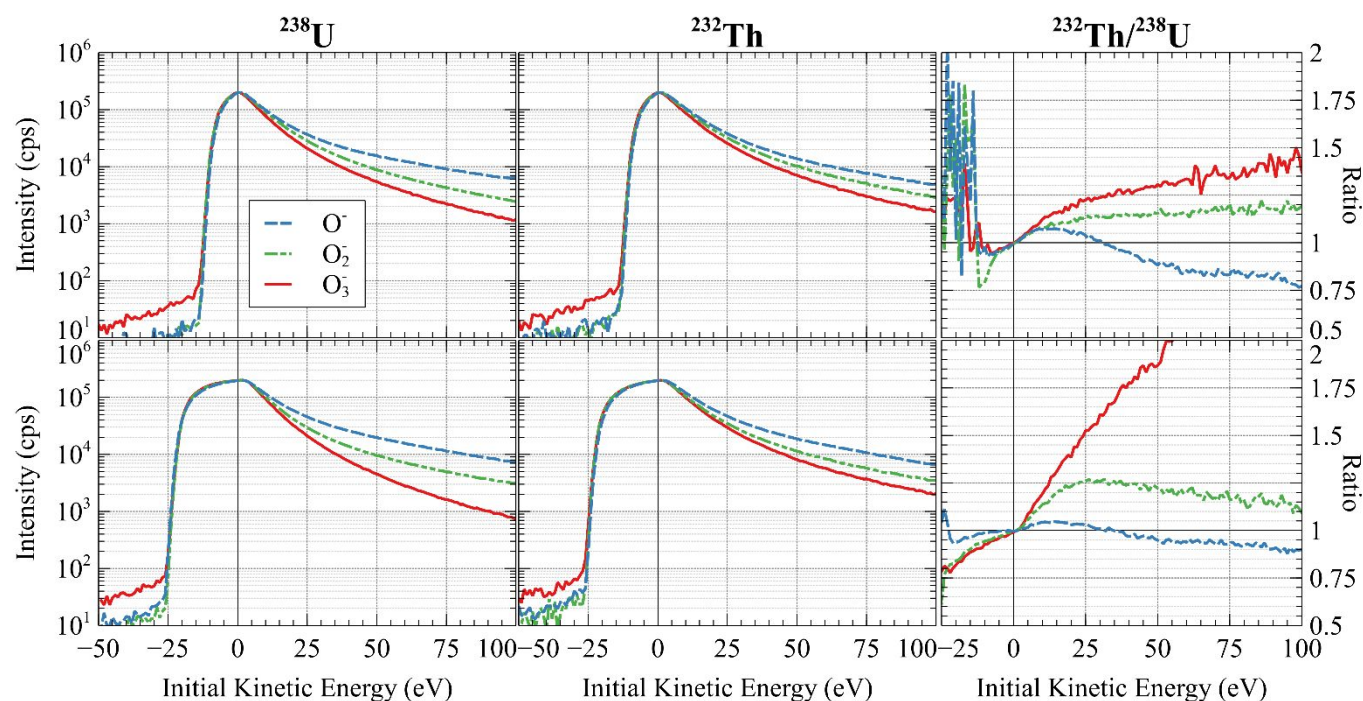**Comparison of U^+, UO^+, and UO_2^+ yields using O^-, O_2^-, and O_3^-**

Figure 6: Energy scans of ^{238}U$^+$ and ^{232}Th$^+$ from uraninite particles on graphite with 10 eV (top) and 25 eV (bottom) bandpass.

Using the multicollector, we measured simultaneous depth profiles of ^{238}U$^+$, ^{238}U^{16}O$^+$, and ^{238}U^{16}O$_2^+$ from CRM U900 particles on both substrates, IRMM 2329P on vitreous carbon, and inkjet particles on Si. Figure 7 shows profiles and molecular ratios from U900 particles for the three beams. Note, all particles were measured with 10 nA primary beams, but due to varying particle sizes the signals could not be converted to useful yields. On graphite, the UO$^+$ signal was initially the most intense for O$^-$ and O$_2^-$ but was eventually overtaken by U$^+$. In contrast, U$^+$ was the most abundant signal throughout the profile for O$_3^-$. UO$_2^+$ was consistently less abundant than U$^+$. The behavior on Si was quite different. For all beams, UO$^+$ was the
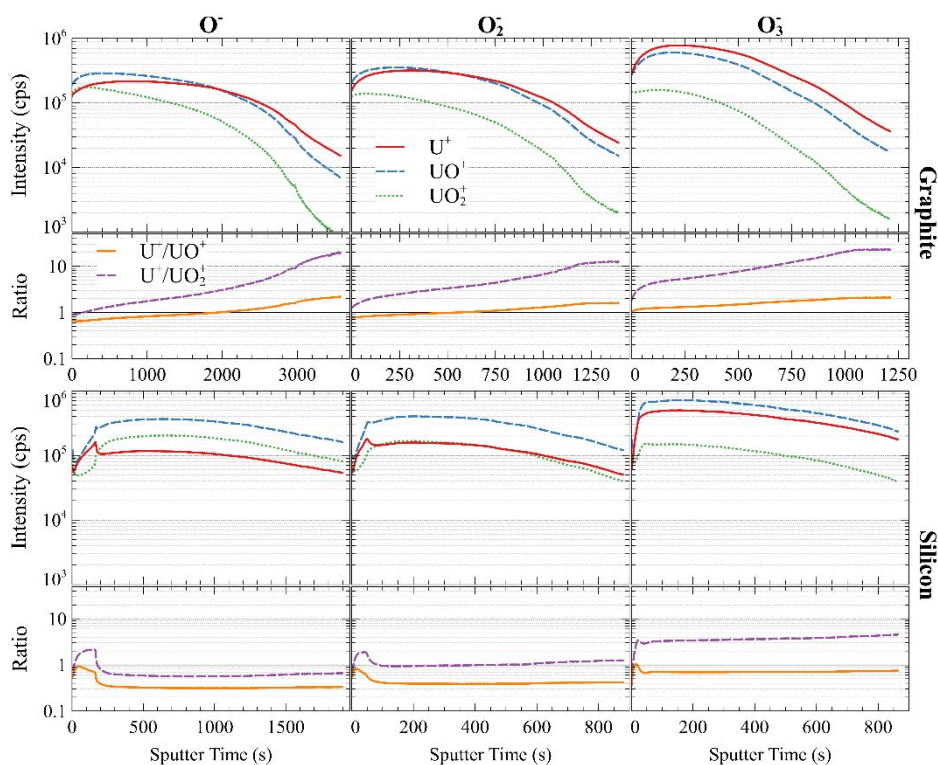

Figure 7: Depth profiles and ratios of U$^+$, UO$^+$, and UO$_2^+$ from U900 particles on graphite and silicon. 10 nA primary intensity. Note: U900 particle sizes are not uniform, so variations in ion intensity were not solely due to yield differences.
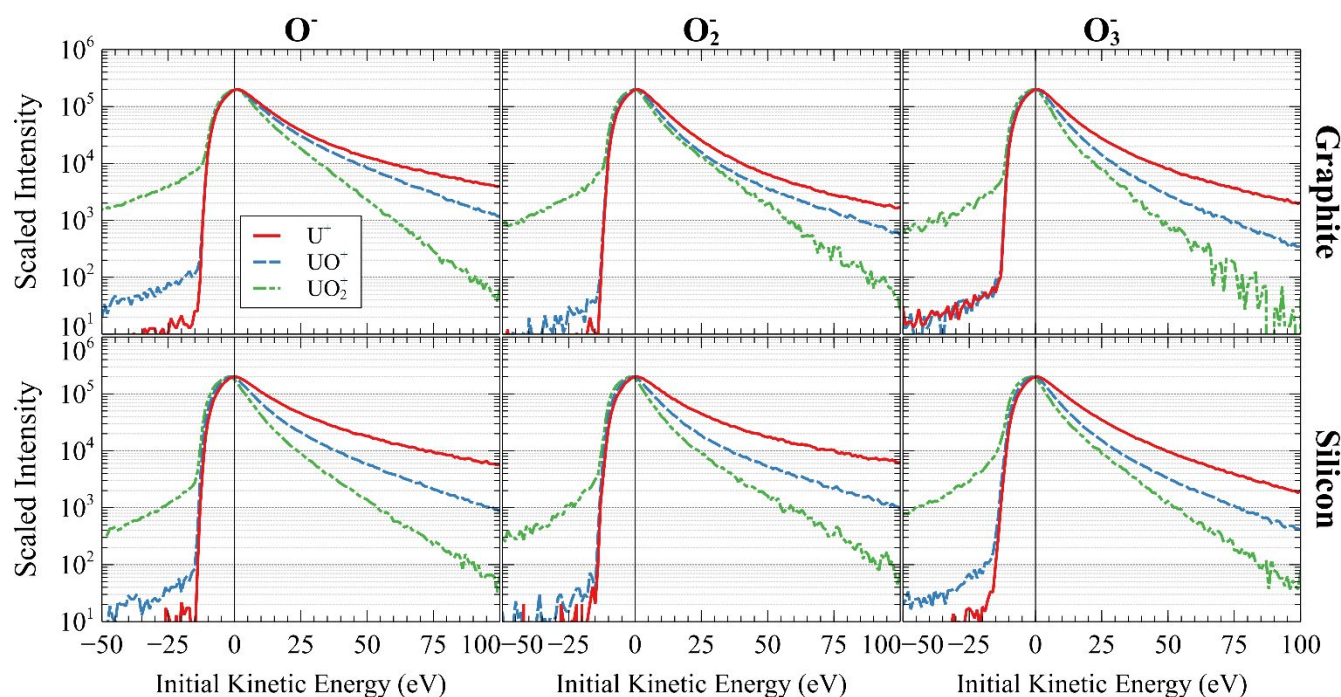
ARTICLE

Figure 8: Energy scans of U^+, UO^+, and UO_2^+ from CRM U900 with a 10 eV energy window.

dominant signal throughout, however the ratio of U^+/UO^+ increased from O^- through O_3^-. The abrupt change in ion yields from the Si $\rightarrow$ SiO$_x$ transition was visible under O^- and O_2^- bombardment, as before, but was absent from O_3^- (or occurred very rapidly at the beginning). The phase transition resulted in a sharp increase in the UO_2^+ signals. Under O^- bombardment, U^+ was the least abundant signal after this transition. With O_2^-, the transition resulted in U^+ and UO_2^+ having comparable intensities. O_3^- resulted in a uniformly lower UO_2^+ yield relative to U^+.

Figure 8 shows the energy distributions of U^+, UO^+, and UO_2^+ measured on U900 with a 10 eV wide energy slit. As before, O_3^- resulted in the narrowest energy distributions for all ions on both substrates. For O_3^- on graphite, the molecular ion distributions were relatively narrower than U^+ on the high-energy side than they were for O^- and O_2^-. Between the substrates, the O_3^- energy distributions were nearly identical. In contrast, there were much larger distribution differences between graphite and Si for O_2^-. On Si, there were $\approx 2 - 3\times$ more high-energy U^+ and UO^+ ions than on graphite. With O^-, there were also more high-energy U^+ ions on Si, though the effect was less pronounced. All combinations showed a low-energy component of the UO_2^+ distribution below the nominal kinetic energy. The peak of the UO_2^+ distribution also appeared to be shifted to lower energy by a few eV. This indicates that some UO_2^+ formed from collisions of ions and neutral atoms above the sample surface, presumably with different ejection angles. For O^- and O_2^-, this low-energy UO_2^+ component was more abundant from particles on graphite than on Si; it was similar for O_3^- on both substrates. This is interesting as it inverts the typical energy-filtering scenario where molecular signals are relatively more suppressed on the high-energy sides of the distributions.

Figure 9 shows the multicollector depth profiles of IRMM 2329P on vitreous carbon and the U^+/UO^+ and U^+/UO_2^+ ratios. As before, O_3^- produced the largest fraction of U^+ ions and the highest overall yield. Note, the "CIRCULAR" tuning required for multicollection has intrinsically less transmission than "XY" mode used for monocollection at the same MRP. The useful yields for O_3^- were U^+: 3.7 ± 0.3 %; UO^+: 2.8 ± 0.3 %; UO_2^+: 0.6 ± 0.1 %. For O_2^- these were U^+: 2.3 ± 0.2 %; UO^+: 2.4 ± 0.2 %; UO_2^+: 0.8 ± 0.1 %. For O^- U^+: 2.2 ± 0.2 %; UO^+: 2.0 ± 0.2 %; UO_2^+: 1.0 ± 0.2 %. Overall, the yields of U^+ and UO^+ increased from O^- to O_3^-, while the yields of UO_2^+ decreased. As shown above, the energy distribution of UO_2^+ was shifted a few eV lower than U^+ and UO^+, but with a 50 eV bandpass this should make an insignificant impact on the yields.

Figure 10 shows the multicollector depth profiles of the inkjet-printed deposits on Si. These profiles showed significant differences compared to the previous samples on both substrates. Interestingly, as the primary ion mass increased, the relative yields of molecular ions decreased while the atomic ion yields increased (note the difference in sputter times). Unlike the other samples, UO_2^+ was the most abundant signal under O^- and O_2^- bombardment, followed by UO^+, with both being nearly $10\times$ larger than U^+. For O_3^-, UO^+ was more abundant than UO_2^+. The behavior of all the signals is interesting before the Si$\rightarrow$SiO$_x$ transition. Unlike the U900 particles on Si, where this transition was accompanied by sharp discontinuities in all three secondary signals (Figure 7), the behaviors of UO^+ and UO_2^+ appear to be impacted less for the inkjet deposits. It appears likely that the unique morphology, density, and/or other characteristics of the inkjet samples on Si play an important role in secondary ion formation. O_3^- produced a U^+ yield enhancement of approximately 50% relative to O^- and O_2^-.
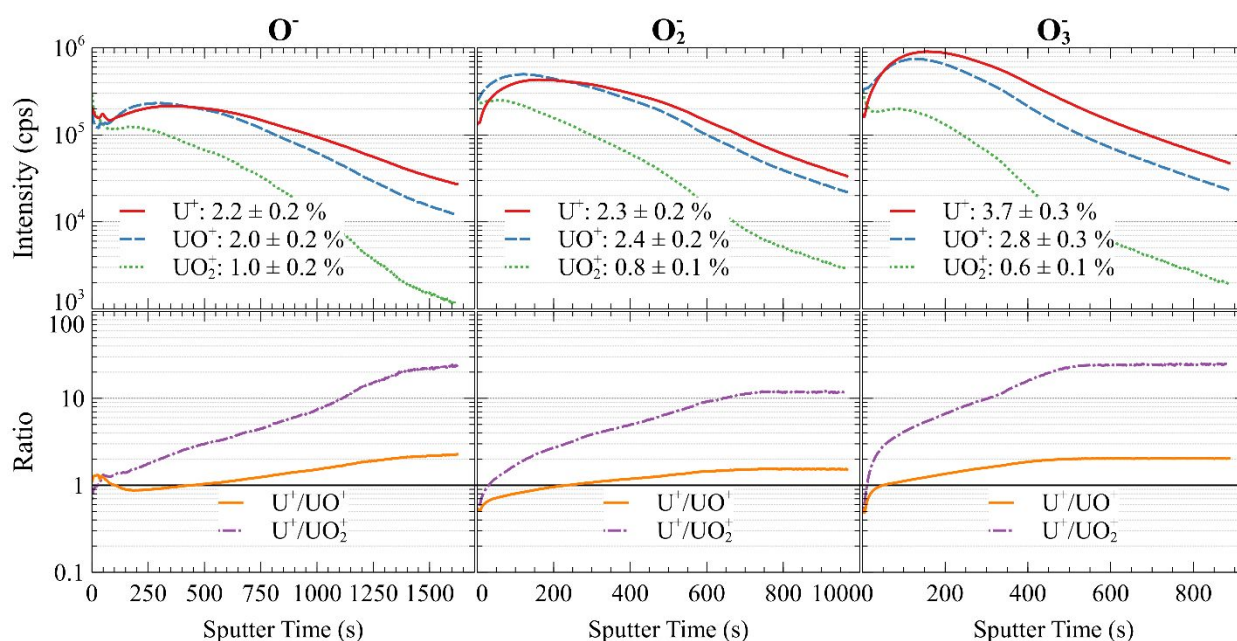
Figure 9: Multicollection depth profiles of IRMM 2329P on graphite under 10 nA Köhler bombardment from O^-, O_2^-, and O_3^-. The relative proportion of $^{238}U^+$, $^{238}U^{16}O^+$, and $^{238}U^{16}O_2^+$ secondary ions vary between beams and over the course of a depth profile. O_3^- yields the largest relative abundance of U^+ and produces the highest useful yield.

Discussion and Conclusions

Several negative primary beam species (e.g., O^-, O_2^-, O_3^-) can be produced in the RF plasma and duoplasmatron ion sources. The RF ion source produces O_2^- and O_3^- beam currents useful for particle analysis using Köhler illumination. The useful yields of U particles on carbon and Si substrates were compared using the three primary ion species and it was found that O_3^- produces significantly more secondary ions ($\approx 2\times$ compared to O^-). This yield enhancement improves the statistical precision of isotopic and U/Th age dating analyses. In addition, O_3^- sputtered $3\times$ faster than O^-, which maximized the signal-to-noise ratio of measurements: higher yield plus shorter duration (less cumulative background). This would be particularly useful for age dating measurements, where the instrument background signal may not be negligible for young and/or small particles [4]. The O_3^- primary beam appeared to minimize the impact of substrate chemistry, which yielded smaller variations between substrates in the Th/U RSF, mass bias, and secondary ion energy distributions relative to the other species. These effects were likely driven by the shallower penetration depth of O_3^- into the sample surface at the same nominal energy. A 23 keV O_3^- ion would partition its energy into thirds (7.66 keV/atom) upon impact, and according to simulations using The Stopping Range of Ions in Matter (SRIM) by James Ziegler [34], each O atom would have an average range of 21 nm in Si. A 23 keV O^- ion would have an average range $\approx 2.5\times$ deeper at 58 nm. O_2^+ was not investigated in this work, but it is known to have a lower secondary ion yield for U^+ than O^- [5, 6]. A 7 keV O_2^+ (+15 kV acceleration minus +8 kV sample bias) ion would partition its energy into two 3.5 keV O atoms each penetrating on average 11 nm into Si.

In contrast to models where mass fractionation is inverse-velocity dependent [32], it was found that O_3^- produced a narrower and lower-average energy distribution than the other primary species, and also resulted in lower mass fractionation. This is similar to work on oxygen isotope fractionation [33] and indicates that another mechanism, such as sample chemistry may be more important. Eiler et al. [33] found a sputter rate dependence for oxygen isotope fractionation from bulk glass samples, however we did not observe any sputter rate dependence here. Future work should explore this mass bias effect more systematically by measuring U isotopes with a narrow energy slit (e.g., 2 eV) at different sample offset voltages. Exploring the mass bias behavior of other elements and substrates would also be informative. Even with the 50 eV energy bandpass used for the isotopic measurements in this paper, the difference in mass bias between the beams and substrates was quantifiable.

For particles on carbon substrates, O_3^- produced mostly atomic U^+ secondary ions and resulted in the highest useful yield (up to 4.7% at MRP = 2000). O_3^- resulted in a nominally identical Th/U RSF to the other primary species. These benefit both monocollector and multicollector analyses of U isotopes and the U/Th chronometer. O^- and O_2^- produced more UO^+. Analyses of UO^+ isotopes have been performed several times using O^- primary beams in attempts to capitalize on potential precision improvements afforded by larger UO^+ ion yields relative to U^+ on some samples [35-38]. However, on substrates or samples containing C and/or F, UO^+ isotope ratios are compromised by interferences, such as overlapping $^{234}U^{16}O^+$ and $^{238}U^{12}C^+$ at m/z $\approx$ 250, which requires a MRP > 25,400 to separate on LG-SIMS, small geometry (SG)-SIMS, and NanoSIMS instruments (this is not practical for any trace analysis). This was not the case for the NRL NAUTILUS, which used an accelerator mass spectrometer to remove interferences and analyze molecular fragments [9]. On non-ideal or real-world
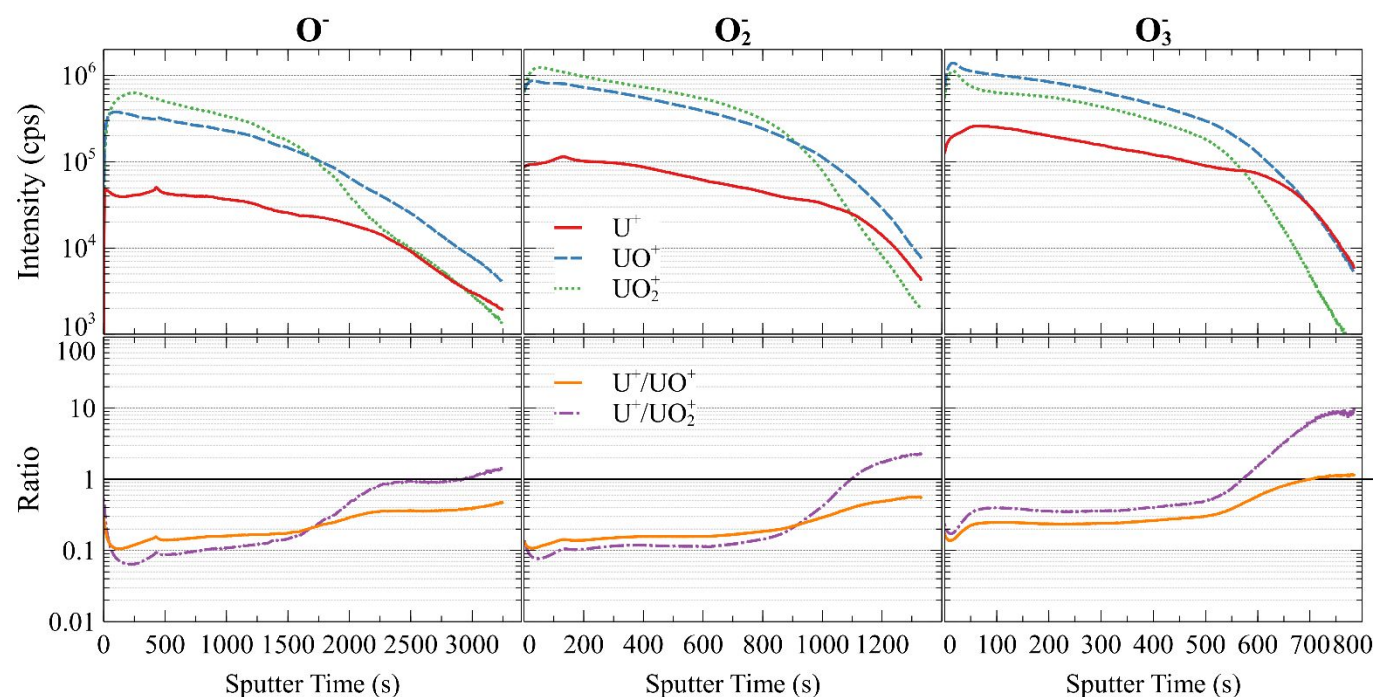
ARTICLE

Figure 10: Multicollector U⁺, UO⁺, and UO₂⁺ profiles of inkjet particles on Si (4 nA primary intensity). Molecular secondary yields were significantly higher than other samples measured indicating potentially unique sample conditions. Identical particles on different substrates are needed for further investigation.

environmental samples, it may be infeasible to monitor and correct for these interferences on conventional SIMS instruments. Carbon is a widespread surface contaminant from organic solvents, oils, resins (e.g., poly(methyl methacrylate), PMMA), and is also present in non-ultrapure Si wafers, and in soils. Likewise, UF_6 is commonly used at uranium enrichment facilities.

For particles on Si, UO_x^+ ions were the most intense signals, though O_3^- increased the relative proportion and overall yield of U^+. As above, however, carbon in the sample or carbides in the substrate could negate the potential benefits of measuring UO^+. Future work could investigate the mass bias and RSF of UO_x^+ and ThO_x^+ signals to determine what precision gains might be realized for interelement U/Th measurements by analyzing molecular ion signals from particles on Si. Due to the rapid phase transition from Si→SiO_x, Si has not been a viable sample substrate for monocollector measurements using O^-. Since O_3^- eliminated the rapid phase change of the Si substrate under oxygen bombardment and correlated secondary signal variations, monocollector measurements with higher instrument transmission would be more feasible than in the past. Extrapolation of the results from the inkjet-printed samples on Si requires some caution, as they may not adequately mimic real-world particle samples, with a large aspect ratio (wider than they are tall).

One of the limitations of the current data sets was the lack of identical, monodisperse particles on the different substrates. CRM U900 particles were not monodisperse or certified for mass, while IRMM 2329P and the inkjet-printed deposits were only available on carbon and Si, respectively. Production of samples with known mass by VOAG, inkjet printing, or hydrothermal solution synthesis[39, 40] on identical substrates

would allow for firmer conclusions regarding the ion yield and energy distribution behaviors of the primary beam species. These samples would also allow for a more systematic study of Köhler spot size (or rastered Gaussian beam area) on the useful yield and the magnitude of matrix effects.

Another avenue for future investigation would be incorporating O_2 and/or other reactive gas flooding of the sample. This has been used in various capacities to increase atomic and/or molecular ion yields, and reduce surface roughening under primary beam bombardment, e.g., [9, 41-47]. However, the addition of gas in the sample chamber can increase collisions with ejected ions and shift the secondary energy spectra of atomic and molecular species. Care should be taken to investigate how the mass fractionation and RSFs evolve in combination with substrate, primary beam species, flooding species, and sample chamber pressure. The energy scans of UO_2^+ showed a low-energy component below the nominal accelerating voltage, potentially indicating molecule formation above the sample surface. This effect was larger on graphite than on Si for O^- and O_2^-, while being nominally the same for O_3^-. This may have implications for energy filtering analyses with or without O_2 flooding and should be explored.

In summary, using O_3^- primary ions provides several benefits relative to other O species: higher U^+ yields, lower mass fractionation, and more consistent results across substrates. For the highest lateral resolution, which benefits particle search analyses, O^- could be preferable on LG-SIMS and SG-SIMS due to its higher brightness relative to the molecular species. However, for single particle analyses using Köhler illumination, the spatial resolution is defined by the last primary beam aperture, so this difference is inconsequential. O_2^+ provides higher depth resolution, in part due to its shallower penetration

depth, however this comes at the expense of secondary signal intensity. For particle measurement this is also unnecessary and of dubious utility in the case of an irregularly shaped particulate. Outside of these specialized cases, O_3^- appears to be the most beneficial primary species to use for U particle and age dating analyses.

Author Contributions

EEG – Conceptualization, data curation, formal analysis, investigation, methodology, software, validation, visualization, writing – original draft
TLW – Investigation, methodology, validation, writing – review & editing
DSS – Validation, writing – review & editing

Conflicts of interest

There are no conflicts to declare.

Acknowledgements

Notes and references

1. D. L. Donohue and R. Zeisler, *Analytical Chemistry*, 2012, **65**, 359A-368A.
2. D. L. Donohue, *Journal of Alloys and Compounds*, 1998, **271-273**, 11-18.
3. A. Axelsson, D. M. Fischer and M. V. Peńkin, *Journal of Radioanalytical and Nuclear Chemistry*, 2009, **282**, 725-729.
4. C. Szakal, D. S. Simons, J. D. Fassett and A. J. Fahey, *Analyst*, 2019, **144**, 4219-4232.
5. Y. Ranebo, P. M. L. Hedberg, M. J. Whitehouse, K. Ingeneri and S. Littmann, *Journal of Analytical Atomic Spectrometry*, 2009, **24**.
6. N. Sharp, J. D. Fassett and D. S. Simons, *J Vac Sci Technol B Nanotechnol Microelectron*, 2016, **34**.
7. P. M. L. Hedberg, P. Peres, F. Fernandes and L. Renaud, *Journal of Analytical Atomic Spectrometry*, 2015, **30**, 2516-2524.
8. P. M. L. Hedberg, P. Peres, F. Fernandes, N. Albert and C. Vincent, *Journal of Vacuum Science & Technology B, Nanotechnology and Microelectronics: Materials, Processing, Measurement, and Phenomena*, 2018, **36**.
9. E. E. Groopman, D. G. Willingham, A. J. Fahey and K. S. Grabowski, *Journal of Analytical Atomic Spectrometry*, 2020, **35**, 600-625.
10. E. E. Groopman and D. G. Willingham, presented in part at the 51st Lunar and Planetary Science Conference, Houston, 2020.
11. L. Pillatsch and T. Wirtz, *Surface and Interface Analysis*, 2012, **44**, 1370-1372.
12. M.-C. Liu, K. D. McKeegan, T. M. Harrison, G. Jarzebinski and L. Vltava, *International Journal of Mass Spectrometry*, 2018, **424**, 1-9.
13. *Certain commercial equipment, instruments or materials are identified in this paper to specify the experimental procedure adequately. Such identification is not intended to imply recommendation or endorsement by the National Institute of Standards and Technology, nor is it intended to imply that the materials or equipment identified are necessarily the best available for the purpose.*
14. P. Williams, H. Abdulkawi, R. Hervig, A. Benninghoven, P. Bertrand, H. Migeon and H. Werner, *Secondary ion mass spectrometry, SIMS*, 2000, **12**, 241-244.
15. S. Clement, W. Compston and A. Benninghoven, *Secondary Ion Mass Spectrometry, SIMS VII. Benninghoven A (ed). J. Wiley & Sons, Chichester*, 1990, 815-819.
16. J. Truyens, M. Dürr, Z. Macsik, R. Middendorp, S. Neumeier, S. Richter, G. Stadelmann, C. Venchiarutti and Y. Aregbe, *CERTIFICATION REPORT: Preparation and Certification of the Uranium Oxide Microparticles IRMM-2329P*, 2020.
17. C. Venchiarutti, S. Richter, R. Middendorp and Y. Aregbe, *NUSIMEP-9: Uranium isotope amount ratios and uranium mass in uranium micro-particles*, Publications Office of the European Union, Luxembourg, 2019.
18. P. Croatto, *U Series Reference Material Production, Age, and Sourcing*, New Brunswick Laboratory, 2014.
19. R. W. Williams, A. M. Gaffney, M. J. Kristo and I. D. Hutcheon, presented in part at the Conference: Presented at: INMM 50th Annual Meeting, Tucson, AZ, United States, Jul 12 - Jul 16, 2009, United States, 2009.
20. D. S. Simons and J. D. Fassett, *J Anal At Spectrom*, 2017, **32**, 393-401.
21. K. Wittmaack, *Surface and Interface Analysis*, 1996, **24**, 389-398.
22. A. E. Morgan, H. A. M. de Grefte, N. Warmoltz, H. W. Werner and H. J. Tolle, *Applications of Surface Science*, 1981, **7**, 372-392.
23. J. Kirchner, Weighted Averages and their Uncertainties, http://seismo.berkeley.edu/≈kirchner/toolkits.html).
24. P. Meier, *Biometrics*, 1953, **9**, 59-73.
25. K. Ludwig, *Berkley Geochronological Centre, Special Publication*, 2012.
26. B. Efron, *Journal of the American Statistical Association*, 1987, **82**, 171-185.
27. D. York, *Earth and Planetary Science Letters*, 1968, **5**, 320-324.
28. D. York, N. M. Evensen, M. L. Martinez and J. D. Delgado, *American Journal of Physics*, 2004, **72**, 367-375.
29. E. E. Groopman, L. R. Nittler, D. G. Willingham, A. P. Meshik and O. V. Pravdivtseva, *Applied Geochemistry*, 2021, **131**.
30. P. J. Rousseeuw and C. Croux, *Journal of the American Statistical Association*, 1993, **88**, 1273-1283.
31. A. Azzalini, *Scandinavian Journal of Statistics*, 1985, **12**, 171-178.

32. H. Gnaser and I. Hutcheon, *Physical Review B*, 1987, **35**, 877.
33. J. M. Eiler, C. Graham and J. W. Valley, *Chemical Geology*, 1997, **138**, 221-244.
34. J. F. Ziegler, M. D. Ziegler and J. P. Biersack, *Nuclear Instruments and Methods in Physics Research Section B: Beam Interactions with Materials and Atoms*, 2010, **268**, 1818-1823.
35. D. Willingham, E. Groopman and L. Sangely, *J Am Soc Mass Spectrom*, 2020, DOI: 10.1021/jasms.0c00097.
36. D. Willingham, E. E. Groopman, K. S. Grabowski and L. Sangely, *Analyst*, 2018, **143**, 5364-5371.
37. N. Zirakparvar, C. Hexel, A. Miskowiec, J. Smith, M. Ambrogio, D. Duckworth, R. Kapsimalis and B. Ticknor, *Minerals*, 2019, **9**.
38. N. A. Zirakparvar, C. R. Hexel, J. B. Smith, A. J. Miskowiec, T. L. Spano and R. Kapsimalis, *Sci Rep*, 2020, **10**, 12285.
39. T. R. Pope, B. W. Arey, M. M. Zimmer, I. DeVore, Michael, M. G. Bronikowski, W. Kuhne, A. T. Baldwin, C. Padilla Cintron, N. C. Anheier, M. G. Warner, M. Wellons and C. A. Barrett, *ESARDA Bulletin*, 2019, Medium: X; Size: 29-38.
40. K. Koh, R. Stene, S. Vogt, T. Pope, A. Albrecht and C. A. Barrett, Virtual, 2021.
41. E. Zinner, *Scanning*, 1980, **3**, 57-78.
42. H. Migeon, *Secondary ion mass spectrometry, SIMS IX. Wiley, Chichester, pp 919922Sharp ZD (1990) A laser-based microanalytical method for the in situ determination of oxygen isotope ratios of silicates and oxides. Geochim Cosmochim Acta*, 1994, **54**, 13531357Simpson.
43. M. J. Whitehouse, B. S. Kamber and S. Moorbath, *Chemical Geology*, 1999, **160**, 201-224.
44. M. Moens, F. C. Adams and D. S. Simons, *Analytical Chemistry*, 2002, **59**, 1518-1529.
45. G. Blaise and M. Bernheim, *Surface Science*, 1975, **47**, 324-343.
46. K. Franzreb, J. Lörinčík and P. Williams, *Surface Science*, 2004, **573**, 291-309.
47. J. Sielanko, J. Filiks, M. Sowa, J. Zinkiewicz and M. Drewniak, *Vacuum*, 1995, **46**, 1459-1460.